Microporous and Mesoporous Materials 401 (2026) 113943

Contents lists available at ScienceDirect

Microporous and Mesoporous Materials

journal homepage: www.elsevier.com/locate/micromeso

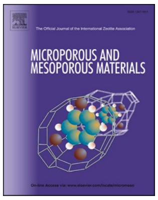

Transition metal docking in MOF-303 for enhanced Atmospheric Water Harvesting: A multiscale simulation approach

Mehrzad Arjmandi [a], Mohamed Khayet [a,b,*], Sofia Calero [c]

[a] Department of Structure of Matter, Thermal Physics and Electronics, Faculty of Physics, University Complutense of Madrid, Avda. Complutense s/n, 28040, Madrid, Spain
[b] Madrid Institute for Advanced Studies of Water (IMDEA Water Institute), Avda. Punto Com N° 2, Alcalá de Henares, Madrid, 28805, Spain
[c] Materials Simulation & Modelling, Department of Applied Physics and Science Education, Eindhoven University of Technology, 5600 MB, Eindhoven, the Netherlands

ARTICLE INFO

Keywords:
MOF-303
Metal docking
Atmospheric water harvesting
Water adsorption
Density functional theory
Multiscale simulation

ABSTRACT

We present a multiscale computational study on water adsorption and transport in pristine and metal-functionalized MOF-303 frameworks for Atmospheric Water Harvesting (AWH). Using Grand Canonical Monte Carlo (GCMC), Kinetic Monte Carlo (KMC), and Molecular Dynamics (MD) simulations, we evaluated the thermodynamic uptake, adsorption kinetics, and mobility of water under varying humidity. Post-synthetic metalation with Cu(I) and Ag(I) increased the hydrophilicity of the framework, with Cu@MOF-303 and Ag@MOF-303 achieving a 37 % and 27 % higher uptake and faster saturation kinetics, respectively. Density Functional Theory (DFT) calculations revealed enhanced binding energies and localized polarization effects at Cu sites, supported by electrostatic potential maps and charge redistribution analyses. Radial distribution function (RDF) analyses revealed that metalation, especially with Cu, enhances water structuring near specific adsorption sites through localized polarization and extended electronic redistribution. Reduced water diffusion in Cu@MOF-303, observed via mean square displacement (MSD) profiles, confirmed stronger confinement. Additionally, temperature-dependent desorption analyses indicated that Ag@MOF-303 offers a more favorable balance between high uptake and moderate regeneration temperatures, reinforcing its practical viability under solar-driven AWH conditions. These results underscore the potential of targeted metal docking to fine-tune MOF performance for water harvesting in low-humidity and off-grid environments.

1. Introduction

Water scarcity is one of the most pressing global challenges facing humanity today [1]. With increasing population growth, industrialization, and climate change, the availability of clean and freshwater resources is rapidly declining. Consequently, finding efficient and sustainable methods to harvest water from the atmosphere has gained attention in recent years [2]. Solar-driven Atmospheric Water Harvesting (SAWH) stands out as a promising solution for obtaining potable water from the ambient air, especially in arid and semi-arid regions [3]. As illustrated in Fig. S1, SAWH works by adsorbing atmospheric moisture at night and releasing it during the day through heat-driven desorption, followed by condensation and water collection. The efficiency of this cycle depends heavily on the adsorbent material used [4,5].

Metal-Organic Frameworks (MOFs) have emerged as a highly attractive class of materials due to their exceptional surface area, tunable porosity, and structural flexibility, making them ideal candidates for water adsorption in SAWH systems [4]. MOFs are a diverse group of materials composed of metal ions or clusters linked by organic ligands [6–9]. Their highly porous structure offers an enormous surface area for the adsorption of water molecules. MOF-303, chemically formulated as {[Al(OH) (PZDC)] with $PZDC^{2-}$ representing 1-H-pyrazole-3,5-dicarboxylate}, exhibits an extended framework structure and is constructed from infinite rod-like secondary building units (SBUs) [10]. These SBUs consist of alternating cis-trans corner-sharing AlO_6 octahedra, interconnected via H_2PZDC linkers [10]. The framework features one-dimensional hydrophilic channels approximately 6 Å in diameter, which support both a highly open architecture and the efficient diffusion of water molecules, key attributes for enhanced water

---

* Corresponding author. Department of Structure of Matter, Thermal Physics and Electronics, Faculty of Physics, University Complutense of Madrid, Avda. Complutense s/n, 28040, Madrid, Spain.
E-mail address: khayetm@fis.ucm.es (M. Khayet).

https://doi.org/10.1016/j.micromeso.2025.113943
Received 29 September 2025; Received in revised form 11 November 2025; Accepted 11 November 2025

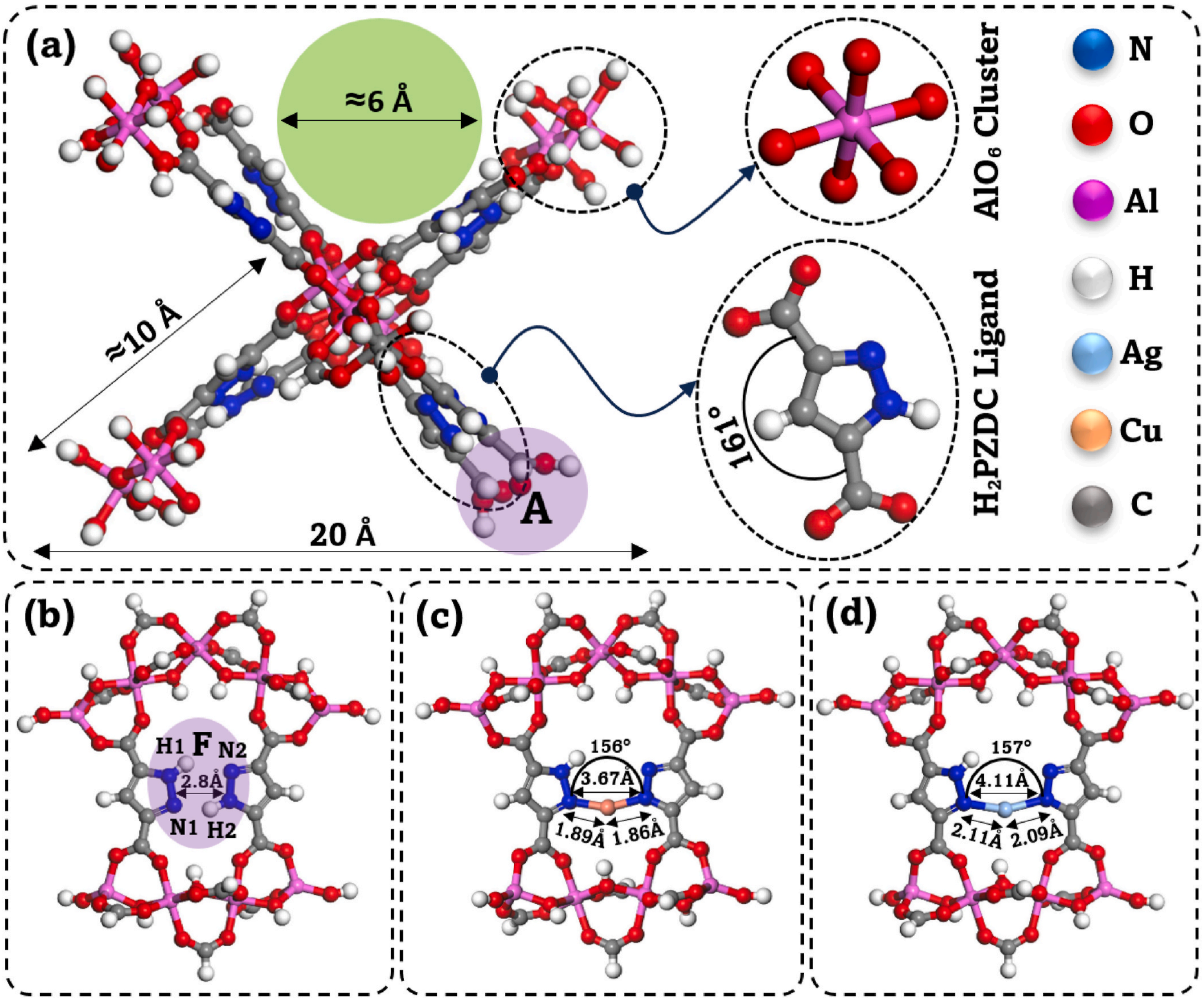

Fig. 1. (a) Structural model used in simulations, showing the pore size. The ligand and metal cluster are also depicted separately. Zone A highlights the organic fragment used to study adsorption behavior without the metal cluster. Simplified DFT models are shown for (b) pristine MOF-303, (c) Cu@MOF-303, and (d) Ag@MOF-303. In all cases, key bond lengths and angles are presented separately.

adsorption performance. MOF-303 displays an exceptional water uptake capacity of up to 0.48 g g^{-1} and outstanding hydrolytic stability, withstanding 150 adsorption–desorption cycles without any detectable structural degradation [11]. Under operational conditions of 30 °C and relative humidity (RH) between 20 and 40 %, MOF-303 achieves its maximum uptake within just 15 min, with adsorption capacities ranging from 0.35 to 0.45 g g^{-1} depending on RH [12,13]. Its practical potential has been validated through integration into water harvesting systems, capable of producing 1.3 L kg^{-1} day^{-1} in controlled indoor environments (32 % RH, 27 °C), and 0.7 L kg^{-1} day^{-1} under desert-like conditions (10 % RH, 27 °C) such as those in the Mojave Desert [13]. MOF-303 can be synthesized on a large scale using various methods, including solvothermal, microwave-assisted, flask reflux, and vessel reflux, achieving up to 3.5 kg per batch with 91 % yield through a rapid, water-based, and environmentally friendly process [14].

MOFs can be tailored at the molecular level to perform efficiently under specific environmental conditions [15]. Functional group modification enhances their water adsorption capacity, selectivity, and stability across varying humidity and temperature [16]. Incorporating external metal ions is an effective strategy, either through coordination with the secondary building units or attachment to organic linkers containing chelating sites such as bipyridyl [16]. Post-synthetic modifications are also commonly used. These strategies and their applications have been reviewed by Li et al. [17]. This structural engineering strategy has been successfully applied to MOF-303 through precise post-synthetic metalation. By leveraging the orientation of uncoordinated nitrogen atoms along the Al-O SBUs, monovalent metal ions such as Cu(I) and Ag (I) were efficiently incorporated into specific chelation sites [16]. The resulting metalated MOF-303 showed excellent xenon adsorption capacity and selectivity, confirming its potential in advanced gas separation. Beyond gas applications, Ag-MOF-303 with reduced pore size was integrated into nanocomposite membranes, leading to improved nanofiltration performance, including better selectivity, antifouling properties, and antibacterial activity [18]. MOF-303 has also served as a platform for immobilizing Cu species for radioiodine capture, where both Cu^{2+} and Cu^{0}-loaded frameworks exhibited high uptake and stability under humid, high-temperature conditions due to dual-pyrazole coordination and active copper sites [19]. While the role of MOF-303 in SAWH is established, the potential of transition metal incorporation to synergistically enhance both water uptake and regeneration efficiency remains unexplored and represents a promising direction for future research.

To investigate the impact of Cu(I) and Ag(I) docking on the structural and adsorption-desorption behavior of MOF-303 in SAWH, a hierarchical multiscale computational framework was employed. This integrated approach combines complementary simulation methods, each addressing a distinct physical scale and property of the water harvesting process. First, Density Functional Theory (DFT) calculations were performed to understand metal-water binding geometries, adsorption energetics, and charge redistribution at the quantum level, thereby supplying the partial atomic charges and binding energy that served as the quantum-scale baseline for parametrizing the subsequent simulations. Using this electronic-level information, Grand Canonical Monte Carlo (GCMC) simulations were employed to obtain equilibrium water adsorption isotherms, which were subsequently quantitatively analyzed using established Langmuir, Sips, and Toth isotherm models to extract adsorption parameters and assess energetic heterogeneity. After that, Kinetic Monte Carlo (KMC) simulations were conducted to capture time-resolved adsorption kinetics, extending the accessible simulation timescales beyond those achievable with standard molecular dynamics. Finally, Molecular Dynamics (MD) simulations were employed to analyze molecular transport and water structuring within the pores. Static properties, including Radial Distribution Functions (RDFs), were used to characterize local water ordering, while diffusion-related descriptors, such as Mean Square Displacements (MSDs) and diffusivity, were calculated to quantify molecular transport. To complete the full SAWH cycle, temperature-dependent desorption analyses were further performed using DFT-derived adsorption energies to evaluate the regeneration temperature and time. This workflow ensures the consistent propagation of information from electronic to macroscopic scales, enabling a more rigorous assessment of water uptake and regeneration efficiency compared to general MC–MD hybrid schemes, which do not explicitly account for either quantum-scale binding energetics or kinetic resolution. While the actual methodological workflow proceeds from DFT to GCMC, KMC, and MD, the order of presentation is arranged to provide a clearer and more intuitive flow from macroscopic adsorption behavior to atomistic, kinetic, dynamic, and thermodynamic insights.

2. Models and methods

2.1. Models

In this study, the three-dimensional crystal structure of MOF-303 was obtained from the Cambridge Crystallographic Data Center (CCDC) [20]. To assess the water adsorption behavior, a central portion of a four-unit-cell supercell was extracted and subjected to MD, GCMC, and KMC simulations, as depicted in Fig. 1a. The extracted region does not represent a complete unit cell but rather a central segment of the supercell large enough to preserve the intrinsic pore geometry and local coordination environment while minimizing edge effects and computational cost. For a more thorough interpretation of the simulation outcomes and to highlight the role of the inorganic cluster and metal coordination, a representative fragment excluding the metal cluster was selected, as indicated by zone A in Fig. 1a. Additionally, for quantum-level analysis, a simplified molecular model shown in Fig. 1 (b–d) was adopted for electronic structure calculations based on DFT. This truncated fragment preserves the essential Al-O coordination geometry and nearby pyrazole linker environment, accurately capturing the local electronic characteristics around the adsorption site, while terminal atoms were fixed to mimic the rigidity of the periodic framework. Although this model accurately captures local metal-ligand interactions and charge redistribution, it does not explicitly account for long-range electrostatic effects inherent to the periodic lattice. All computational procedures were performed on corresponding metalated MOF-303 models, alongside the pristine structures. Cu(I) and Ag(I) ions are docked at specific sites formed by pairs of adjacent uncoordinated nitrogen atoms on the pyrazole dicarboxylate linkers within MOF-303. Previous experimental studies demonstrate that these sites provide a precise and stable coordination environment for these metal ions [16]. The spatial arrangement of these nitrogen atoms along the rod-shaped Al-O secondary building units in MOF-303 create distinct metal binding sites, which are confirmed by 3D electron diffraction and X-ray absorption spectroscopy techniques. Thus, the docking locations chosen in this study align with experimentally validated metalation sites in MOF-303. It is important to note that, to isolate the intrinsic effect of the metal center itself, no additional ligands (e.g., halides or anionic species such as NO_3^-) were included in the metal coordination sphere. This modeling strategy allows for a clearer interpretation of how the metal identity alone modulates the electronic environment and adsorption characteristics, independent of secondary ligand effects.

2.2. Density Functional Theory calculations

To elucidate the interaction mechanisms between water molecules and the pristine MOF-303 as well as the metalated MOF-303 structures, a comprehensive set of DFT calculations was carried out using the Gaussian 16W software package. All calculations were performed at the B3LYP level of theory using a combination of SDD and LANL2DZ basis sets, which provides a reliable compromise between computational cost and accuracy for transition-metal-containing MOF cluster models [21–24]. To represent the extended periodic structure of MOF-303, cluster models were constructed by extracting chemically relevant fragments from the crystal structure. The terminal atoms were constrained to their crystallographic positions to simulate the rigidity of the periodic framework, while the remaining atoms were allowed to relax during full geometry optimization. Following geometry optimization, harmonic vibrational frequency calculations were performed to confirm that all structures corresponded to true minimum on the potential energy surface, as indicated by the absence of imaginary frequencies. The strength of water adsorption was estimated by calculating the single point energy as follows:

$$E_{ads} = E_{MOF+water} - (E_{MOF} + E_{water}) \tag{1}$$

where $E_{MOF+water}$ is the total energy of the water-MOF complex, E_{water} is the total energy of the isolated water molecule, and E_{MOF} is the total energy of the isolated MOF [25,26].

Furthermore, a series of electronic structure analyses were conducted to gain deeper insight into the electronic properties of the system. Molecular Electrostatic Potential (MEP) maps were generated to visualize regions of electrophilicity and nucleophilicity on the surface of the pristine and metaled MOF structures. To further assess the intrinsic electronic properties of the frameworks, Natural bond orbital (NBO) and Mulliken population analysis were performed to examine the internal charge distribution and the delocalization effects induced by metal incorporation. Additionally, dipole moment (DM), was computed for the optimized MOF structures to quantify the influence of functionalization on molecular polarity. Finally, quantum chemical global descriptors derived from the energies of the Highest Occupied Molecular Orbital (HOMO) and the Lowest Unoccupied Molecular Orbital (LUMO) were calculated within the framework of conceptual DFT. These descriptors provide qualitative insight into the system's electronic stability and chemical reactivity [26–29]. Table S1 summarizes the definitions and theoretical significance of each parameter.

2.3. Grand Canonical and kinetic Monte Carlo modeling

While RASPA [30] is a widely recognized platform for Monte Carlo simulations in porous materials, this study employed LAMMPS simulation package to enable seamless integration of GCMC, KMC, and MD simulations (see section 2.4) within a unified, high-performance environment. The choice was motivated by the need to model not only equilibrium adsorption isotherms, but also time-resolved adsorption kinetics and dynamic confinement effects induced by metal doping.

LAMMPS supports flexible scripting of kinetic models, hybrid MC-MD simulations, and direct implementation of residence-time algorithms for rare-event sampling. This multiscale simulation pipeline allowed us to resolve both the thermodynamic and kinetic contributions to water uptake and retention in pristine and metal-functionalized MOF-303, providing molecular-level insight into structure-performance relationships under realistic operating conditions. The simulation workflow was fully automated via a custom Python script that generated system configurations based on different conditions. OVITO (Open Visualization Tool) was employed throughout the simulation workflow, including the preparation of LAMMPS input data files and the generation of three-dimensional atomic configurations across multiple GCMC simulation timesteps. This allowed both structural setup and dynamic adsorption behavior to be visualized and analyzed effectively. Water molecules were allowed to undergo translation, rotation, reinsertion, and swap moves. The MOF-303 frameworks were treated as rigid during all simulations. Interatomic interactions were described using a combination of 12-6 Lennard-Jones (L-J) and Coulombic potentials, following the equation [10,31]:

$$U_{unbound} = 4\varepsilon_{ij}\left[\left(\frac{\sigma_{ij}}{r_{ij}}\right)^{12} - \left(\frac{\sigma_{ij}}{r_{ij}}\right)^{6}\right] + \frac{q_i q_j}{4\pi\varepsilon_0 r_{ij}} \tag{2}$$

$$\varepsilon_{ij} = \sqrt{\varepsilon_i \varepsilon_j} \tag{3}$$

$$\sigma_{ij} = \frac{\sigma_i + \sigma_i}{2} \tag{4}$$

where σ_{ij} is the L-J collision diameter, ε_{ij} is the L-J well depth, r_{ij} is the distance between atoms i and j, q is the charge of each atom, and ε_0 is the permittivity of vacuum. The Lorentz-Berthelot combination rules were applied to define interaction parameters between non-identical atom pairs. L-J interactions were truncated and shifted at 12 Å, while long-range electrostatics were treated using the Ewald summation method, with a precision of 10^{-6}. The pristine and metalated MOF-303 force field parameters were assigned based on a combination of the DREIDING [32] and UFF force field [33]. Partial atomic charges were obtained through Gaussian software package with the charge-equilibration method. Water molecules were represented using the SPC/E model [34].

KMC simulations were employed to model the time-resolved evolution of water adsorption-desorption and diffusion in both pristine and metalated MOF-303 frameworks [35,36]. The KMC algorithm utilized a residence-time algorithm based on the Bortz-Kalos-Lebowitz (BKL) method to simulate rare events over extended time scales, enabling the exploration of dynamic behavior such as surface hopping, clustering, and site-to-site transport with chemical specificity. Transition probabilities for elementary events were calculated from thermodynamic parameters obtained via DFT calculations and GCMC simulations, with rate constants determined by the Arrhenius equation [37]:

$$K_i = A_i.\exp\left(\frac{-E_i}{RT}\right) \tag{5}$$

where A_i denotes the pre-exponential factor, E_i the activation energy, R the universal gas constant, and T the absolute temperature. This framework enabled efficient sampling of rare events and a realistic description of diffusion pathways, surface hopping, and site-specific interactions over extended timescales.

2.4. *Molecular dynamic modeling*

Molecular dynamics (MD) simulations were employed to investigate the time-resolved behavior of water molecules within both the pristine and metalated MOF-303 frameworks under ambient conditions. Simulations were conducted in the NVT ensemble using the LAMMPS software, treating the frameworks as rigid and modeling water molecules with full flexibility. During the simulation, the temperature of the system was effectively controlled using the Nose–Hoover thermostat [38]. All simulation steps were automated and analyzed via Python scripting, using the MD Analysis package for trajectory handling and VMD for visualization.

From the trajectories generated, various structural and dynamic descriptors were analyzed. Specifically, radial distribution functions (RDFs) [39,40] were computed between the oxygen atoms of water molecules (Ow) and atoms at distinct adsorption sites within zone F (as illustrated in Fig. 1b) of both pristine [10] and metalated MOF-303 structures. These analyses were conducted at two representative pressures, 250 Pa and 700 Pa, corresponding to conditions before and after the sharp adsorption step. The RDF was calculated using the standard expression:

$$RDF(r) = \frac{n_{r+dr}}{4\pi r^2 \rho dr} \tag{6}$$

where r is the distance from a reference atom, n_{r+dr} is the number of atoms in the spherical shell between r and $r + dr$, and ρ is the average atomic density.

Furthermore, the mean square displacement (MSD) of water molecules was computed to probe their translational dynamics within both pristine and metalated MOF-303 frameworks. This analysis allows quantification of molecular motion under confinement and provides insight into water mobility. The detailed formulation of MSD and the subsequent calculation of the self-diffusion coefficient (D) using Einstein's relation are provided in the Supplementary Information (Eqs. S1 and S2) [41,42].

2.5. *Thermodynamic and kinetic analysis of desorption*

To evaluate the temperature-dependent desorption process, thermal corrections were applied to the adsorption energy by accounting for translational, rotational, and vibrational contributions [43]. In this study, the thermal contributions were computed using scaled DFT vibrational frequencies within the harmonic approximation [44–46], while translational and rotational contributions were treated using classical approximations [46]. These approximations provide a practical way to include the main effects of molecular motion on desorption energies and kinetics at typical temperatures. This yields a temperature-corrected desorption energy, $E_{des}(T)$, reflecting increased molecular motion at higher temperatures. It is important to emphasize that this approach is an approximation. Translational and rotational contributions were treated classically, neglecting quantum effects, while vibrational contributions were evaluated using scaled DFT harmonic frequencies. Possible anharmonicities and other higher-order quantum effects are not considered, and thus the thermal corrections may slightly over- or underestimate the true values in some cases. Despite these limitations, this approach captures the dominant trends and provides a computationally efficient way to incorporate temperature effects, sufficient for estimating regeneration temperatures and desorption times within the complete SAWH cycle. Detailed technical descriptions and the specific formulas used are provided in the Supplementary Information (Eqs. S3–S5). The desorption time, *(T),* estimated using the Polanyi-Wigner expression derived from transition-state theory (TST) [47]:

$$\tau(T) = \vartheta_0^{-1}.\exp\left(\frac{-E_{des}(T)}{K_B T}\right) \approx \vartheta_0^{-1}.\exp\left(\frac{-E_{ads}(T)}{K_B T}\right) \tag{7}$$

where ν_0 is the attempt frequency, K_B is the Boltzmann constant. As temperature increases, thermal motion in both the MOF framework and water molecules leads to reduced adsorption strength and faster desorption dynamics. Within the framework of TST, the desorption activation energy (E_{des}) is approximated by the absolute value of the adsorption energy ($|E_{ads}|$), since desorption is the reverse process of adsorption and involves overcoming the same binding energy barrier.

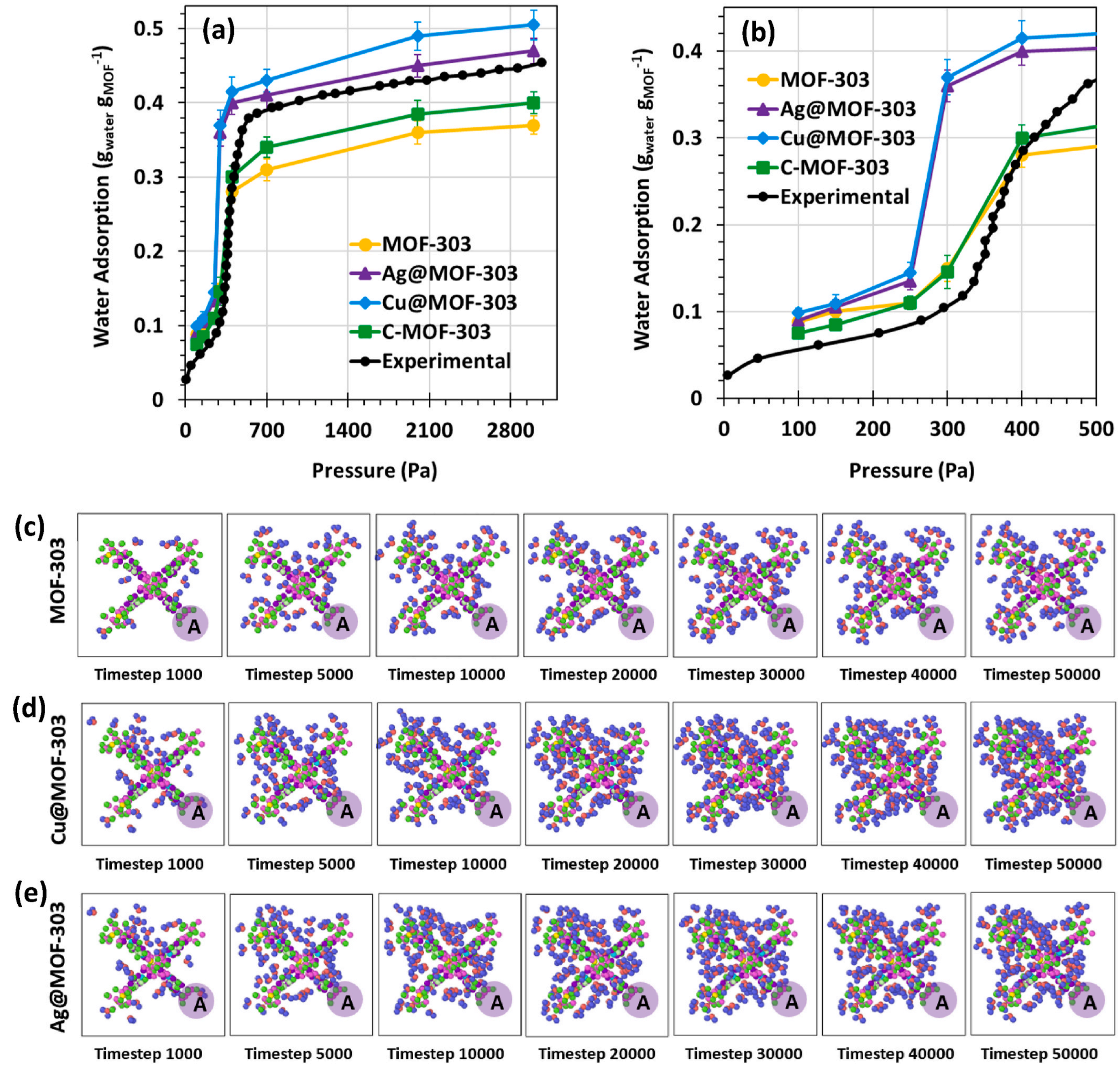

Fig. 2. GCMC water adsorption isotherms for pristine MOF-303 and X@MOF-303 (X = Cu, Ag) at 300 K: (a) full range; (b) low-pressure region ($P \leq 500$ Pa). Time-resolved 3D snapshots of water adsorption at 3000 Pa and 300 K for (c) MOF-303, (d) Cu@MOF-303, and (e) Ag@MOF-303.

This approximation has been widely employed in adsorption-desorption kinetics models for adsorption systems [47–50].

3. Results and discussion

3.1. Water adsorption behavior

The water adsorption isotherms derived from GCMC simulations for pristine MOF-303 and its metal-docked variants are presented in Fig. 2a and b, alongside experimental data from Ref. [51] for validation. The simulated isotherm based on the simplified structural model (corresponding to Fig. 1a) captures the general trend observed experimentally-namely, a gradual uptake at low relative pressures followed by a steep increase at higher pressures-capturing the qualitative shape of the experimental isotherm of the hydrophilic pore environment. The absolute adsorption capacity is consistently underestimated due to the model's structural simplification, especially the exclusion of the full inorganic cluster in zone A, which is important for stabilizing water molecules.

To further investigate this effect, an extended structural model (C-MOF-303) incorporating the complete Al-O inorganic cluster was simulated. The resulting isotherm showed a notable increase in adsorption capacity and exhibited much closer agreement with experimental measurements. This confirms that the presence of the Al-O nodes significantly enhances water-framework interactions, providing high-energy binding sites that become populated at lower relative pressures and steepen the isotherm response.

Post-synthetic incorporation of Cu(I) and Ag(I) ions into the framework increased water uptake. The capacity of Cu@MOF-303 and Ag@MOF-303 was about 37 % and 27 % higher than pristine MOF-303, respectively. At ultra-low humidity conditions (around 10 % RH), the adsorption is dominated by strong primary binding sites located near the Al-O clusters and metal-docking regions. The GCMC simulations show that in this situation, pristine MOF-303 exhibits a limited uptake of approximately 0.15 g g^{-1}. In contrast, Ag@MOF-303 and Cu@MOF-303 demonstrate markedly enhanced adsorption capacities of about 0.367 g g^{-1} and 0.372 g g^{-1}, corresponding to 145 % and 148 % increases over the pristine framework, respectively. This improvement is attributed to the increased local polarity and charge density introduced by the metal centers, which facilitate stronger electrostatic and coordinative interactions with water molecules. Cu@MOF-303 showed superior performance, indicating stronger water affinity and a more favorable coordination environment. This enhancement likely arises from the combined effects of Cu(I)'s higher Lewis acidity compared to Ag(I) [52, 53] and the possible formation of transient Cu-H_2O coordination motifs, which promote efficient water clustering and uptake dynamics within the pores.

To quantitatively assess the adsorption behavior and validate the reliability of the simulation results, both experimental and GCMC-derived adsorption data were further analyzed using three established isotherm models: Langmuir [54], Sips [55], and Toth [56]. The detailed equations, fitting parameters, and statistical coefficients for all isotherm models are provided in the Supplementary Information (Eqs. S5-S8), along with model descriptions. The Langmuir model, which assumes a homogeneous monolayer adsorption mechanism, exhibited the lowest accuracy for the metal-docked frameworks (Cu@MOF-303 and Ag@MOF-303), with R^2 values below 0.83, indicating that this simple model cannot adequately represent the energetic and structural heterogeneity introduced by metal incorporation. In contrast, the Sips and Toth models, which account for distributions of adsorption energy, provided substantially better fits ($R^2 > 0.9$) to both experimental and simulation data. The heterogeneity parameter n, extracted from the Sips and Toth models, increased upon Cu(I) and Ag(I) docking, confirming the generation of multiple adsorption sites with varying binding strengths. This effect was particularly pronounced in the Toth model, which exhibited a markedly larger increase in n, indicating stronger heterogeneity and sharper energetic contrasts between different adsorption sites. The equilibrium constants K (pa^{-1}) derived from all three models were found to increase upon metal docking, indicating stronger initial water-framework interactions and higher binding affinity of the adsorption sites. The fitted parameters confirmed that the adsorption capacity (q_m) follows the order Cu@MOF-303 > Ag@MOF-303 > C-MOF-303 > MOF-303, consistent with the trends observed from GCMC simulations. These correlations highlight that metal incorporation not only enhances overall water uptake but also increases the energetic diversity of adsorption sites, leading to stronger and more complex water-framework interactions.

Time-resolved snapshots illustrating water adsorption within pristine and metalated MOF-303 structures at a constant pressure of 3000 Pa are depicted in Fig. 2c–e. In the pristine MOF-303 framework (Fig. 2c), a progressive occupation of the hydrophilic channels is evident throughout the simulation timeline. Nevertheless, the total number of adsorbed water molecules remains relatively limited. Notably, zone A remains predominantly vacant across all snapshots, underscoring the pivotal role of Al-O inorganic nodes as the principal adsorption sites due to their polar character and coordinative unsaturation.

In contrast, the metalated frameworks (Fig. 2d and e) demonstrate markedly enhanced water uptake rates and more substantial pore occupancy at each recorded timestep. This pronounced improvement can be attributed to the incorporation of Cu(I) and Ag(I) ions, which introduce supplementary binding sites and elevate the overall hydrophilicity of the frameworks. These metal centers function as a secondary adsorption site, thereby facilitating accelerated nucleation and aggregation of water molecules within the porous channels. Consistent with observations in pristine MOF-303, the persistent absence of water molecules in zone A across all metalated models further corroborates the indispensable contribution of the inorganic cluster in governing adsorption phenomena. Comparatively, Cu@MOF-303 (Fig. 2d) exhibits a more rapid and extensive accumulation of water molecules, characterized by the formation of densely packed clusters in proximity to Cu sites. This behavior is attributed to the greater positive NBO and Mulliken charge distribution around Cu(I) compared to Ag(I), which enhances its ability to attract water dipoles through stronger electrostatic interactions (see Section 3.2). Although Ag@MOF-303 (Fig. 2e) displays enhanced adsorption compared to the pristine framework, its overall pore filling and molecular density remain inferior to those observed in the Cu-docked analogue. Collectively, these snapshots and their analysis substantiate that metal docking-particularly with Cu-profoundly augments the water adsorption capacity of MOF-303 by furnishing favorable coordination environments and expediting the dynamic filling of hydrophilic channels.

3.2. Structural and electronic Fingerprint

To deepen the understanding of the water adsorption mechanism, we complemented our GCMC-derived isotherms with quantum mechanical DFT calculations. As previously visualized in Fig. 1b, the water-accessible region, labeled as Zone F, was subdivided into two sub-regions: the upper F zone and the lower F zone, based on the spatial distribution of adsorption sites. Table 1 summarizes the computed adsorption energies (E_{ads}) for each sub-region across all studied systems. The adsorption energy results obtained for the pristine MOF-303 structure in the selected framework section used in this study, alongside the previously reported values for MOF-303 [10], showed that, although slight numerical differences exist-attributable to structural model variations and computational methodologies-the general trend of water binding strength across the upper and lower sub-regions of Zone F is consistent between the two datasets.

Turning to the metalated MOF-303s, a clear distinction emerges. For Cu@MOF-303, water adsorption was significantly more favorable in the lower zone ($E_{ads} = -129.86$ kJ mol^{-1}) compared to the upper zone (-102.80 kJ mol^{-1}). This pronounced difference highlights the strong local enhancement of water binding in the vicinity of the Cu site, attributable to its high charge density and polarizing power, which in turn increases the local electrostatic potential and stabilizes water–framework interactions. In contrast, Ag@MOF-303 also exhibited stronger adsorption in the metal-containing lower zone ($E_{ads} = -113.01$ kJ mol^{-1}), compared to the upper zone (-107.09 kJ mol^{-1}), but the enhancement was more moderate relative to the Cu-doped system. This comparison confirms that while both metal ions increase local hydrophilicity, Cu is more effective in promoting strong, localized adsorption interactions due to its superior electron-withdrawing capability and the

Table 1
Adsorption energies of water molecules in upper and lower sub-regions of Zone F.

Adsorbent	$E_{ads}^{Upper\ F\ Zone}$ (kJ mol^{-1})	$E_{ads}^{Lower\ F\ Zone}$ (kJ mol^{-1})	$\overline{E}_{ads}^{F\ Zone}$ (kJ mol^{-1})
MOF-303 (Ref. [10])	∼ −67.05 (Average of Site I and III)	∼ −71.66	∼ −69.35
MOF-303 (This study)	−77.65 ± 0.9	−79.08 ± 0.4	−78.36
Cu@MOF-303	−102.80 ± 1.2	−129.86 ± 0.2	−116.33
Ag@MOF-303	−107.09 ± 1	−113.01 ± 0.2	−110.05

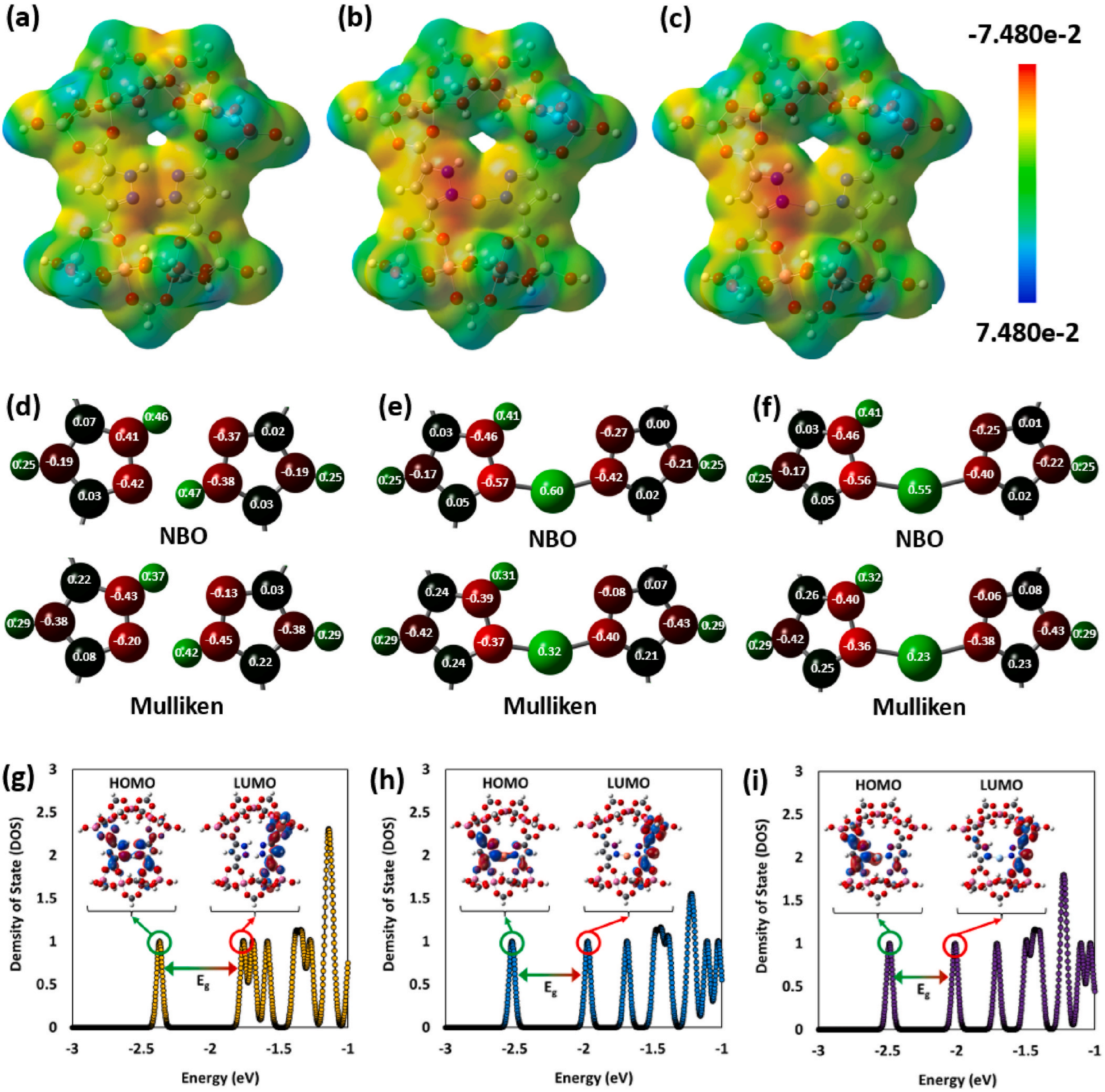

Fig. 3. MEP Surfaces for (a) Pristine MOF-303, (b) Cu@MOF-33, and (c) Ag@MOF-303. NBO and Mulliken Charge Distributions in (d) Pristine MOF-303, (e) Cu@MOF-303, and (f) Ag@MOF-303. Electronic structure analysis of pristine and metalated MOF-303: (g) MOF 303, (h) Cu@MOF-303, and (i) Ag@MOF-303. Each panel shows the DOS diagram along with HOMO and LUMO orbital visualizations, highlighting the effect of metal coordination on frontier orbital distribution and energy gap narrowing.

resulting electrostatic environment. Interestingly, a notable observation emerges in the upper F zone-the sub-region that does not directly host the doped metal center. In this region, Ag@MOF-303 exhibits a stronger adsorption energy (-107.09 kJ mol^{-1}) compared to Cu@MOF-303 (-102.80 kJ mol^{-1}), suggesting that the electronic influence of Ag may propagate more uniformly across the framework, possibly affecting neighboring adsorption sites even in the absence of direct coordination. This behavior points toward a more delocalized modification of the electrostatic environment by Ag, as opposed to the more localized, high-intensity effect seen in Cu. These spatial variations highlight the importance of moving beyond adsorption energetics towards deeper analyses.

However, the average adsorption energy in Zone F for Cu@MOF-303 is -116.33 kJ mol$^{-1,}$ which is more negative than the -110.05 kJ mol^{-1} observed for Ag@MOF-303, indicating a stronger water affinity of the Cu-functionalized framework. The adsorption energies obtained from the DFT cluster model primarily describe local interactions near the adsorption site. Long-range electrostatic contributions present in the extended framework may slightly modify the absolute values but are not expected to affect the observed comparative trends between pristine and metalated MOF-303. These findings are in full agreement with the GCMC isotherms, confirming enhanced uptake capacity in the presence of Cu.

The MEP analysis was employed to gain deeper insight into the three-

Table 2
Dipole moment and Global electronic descriptors for pristine and metalated MOF-303.

Adsorbent	DM (D)	E_g (Hartree)	*IP* (Hartree)	μ (Hartree)	ω (Hartree)
MOF-303	2.137	0.022	0.087	−0.076	0.257
Cu@MOF-303	6.178	0.020	0.093	−0.082	0.338
Ag@MOF-303	6.620	0.017	0.091	−0.083	0.391

dimensional electronic and topological characteristics of the compounds under study. This method enables a visual interpretation of how electron density is distributed across the molecular surface, offering clues about regions that are more likely to participate in electrophilic or nucleophilic interactions. The MEP surface is depicted using a continuous color scale, where blue areas signify regions of electrostatic deficiency (positive potential) and red areas highlight regions of electron accumulation (negative potential). Particularly, red zones are indicative of sites with elevated electron density, which tend to interact favorably with electrophilic species. Fig. 3a–c illustrates the MEP profiles for MOF-303 in both its unmodified form and after metalation with transition metals Cu and Ag. In the pristine framework (Fig. 3a), the potential surface appears relatively uniform and symmetrical. Slightly negative regions are observed in the cavity between ligands. Meanwhile, the ligand's aromatic rings display mostly neutral or weakly negative potential (yellow hues). Upon incorporation of Cu or Ag (Fig. 3b and c), the MEP surface undergoes significant alteration. Strong red and orange zones emerge around the coordinated metal centers and their adjacent donor atoms, revealing an increase in localized negative charge density. This redistribution arises from electron donation by the ligand to the metal center, complemented by potential back-donation from the metal's d-orbitals. The result is a polarized coordination environment with marked asymmetry in the electrostatic potential, especially near the metal-ligand interface. Similar electrostatic patterns-characterized by intense negative potential surrounding metal centers-have been reported for transition-metal complexes [57–64]. These findings, as noted in prior studies, are typically attributed to strong metal-ligand interactions, intramolecular charge redistribution, and enhanced electron delocalization upon coordination [65–67]. The resulting charge polarization not only reshapes the molecular electrostatic environment but may also influence key properties such as chemical reactivity, and site selectivity performance.

Fig. 3d–f illustrates the Mulliken and NBO charge distributions for the pristine MOF-303 and its metaled derivatives. As expected, the transition metal centers (Cu and Ag) exhibit a net positive charge, consistent with their role as electron acceptors in the coordination framework. Notably, the Cu center displays a higher positive charge compared to Ag, reflecting its greater electronegativity and stronger electron-withdrawing character within the framework. This observation suggests a more pronounced ligand-to-metal charge transfer in the Cu-coordinated system. In addition, a comparison with the pristine MOF reveals clear alterations in the atomic charges of donor atoms following metal coordination. The nitrogen atoms directly involved in metal binding show a marked shift in their assigned charges, confirming their participation in electronic reorganization. Similar changes are also observed in neighboring Carbon and Hydrogen atoms within the ligand framework. These variations indicate a redistribution of electronic charge. The overall pattern aligns with the electrostatic perturbations observed in the MEP analysis and underscores the localized polarization induced by metal incorporation.

While Cu and Ag atoms with positive charge and a strong electrostatic field around their coordination sites are commonly associated with water adsorption due to their interaction with the lone pairs of water's oxygen atom, regions of negative potential in Fig. 3a–c can also significantly contribute to water binding [68–73]. These red zones can engage in hydrogen bonding with the partially positive hydrogen atoms of water molecules. Therefore, the centrality of the metal site and the electronic environment surrounding it can act as key determinants of local polarity and interaction type, enabling water molecules to engage either through coordination to electron-deficient metal centers or via hydrogen bonding with electron-rich donor atoms. Thus, both sections may define distinct but complementary interaction modes with water, depending on the nature of the binding site.

While localized analyses of atomic charges and electrostatic potentials provide valuable insights into site-specific interactions and partially explain the differences in adsorption behavior between copper and silver, these methods inherently focus on local electronic environments. To achieve a more holistic understanding of the MOF's electronic structure and its influence on water adsorption, we extend our investigation into the molecular dipole moment, and other global electronic descriptors derived from molecular orbital theory, as shown in Table S1. The summarized results, presented in Table 2 and Table S3, offer comprehensive insight into how the entire electronic framework modulates adsorption properties beyond localized charge effects, facilitating a more complete interpretation of the observed adsorption energies.

The comprehensive analysis of these electronic descriptors reveals profound alterations in the MOF's electronic structure upon functionalization with transition metals, underscoring the significant role of metal docking in modulating the framework's properties. The pronounced increase in dipole moment from 2.137 D in the pristine MOF to over 6 D upon metal incorporation highlights the induction of substantial electronic asymmetry and polarity, which is expected to enhance the interaction with polar adsorbates such as water. Concurrently, the observed decrease in the HOMO-LUMO energy gap signifies improved electronic conductivity and chemical reactivity, facilitating electron transfer essential for adsorption processes. Metal coordination also slightly raises the ionization potential while boosting electron affinity and electronegativity, collectively reflecting a stabilized yet more electron-accepting environment within the framework. Further insights are drawn from the notable reduction in chemical hardness alongside a marked increase in softness, indicative of enhanced polarizability and chemical flexibility following metal introduction. This is complemented by a significant rise in electrophilicity index and both electron donating and accepting powers, portraying the metal-coordinated MOFs as more dynamic electronic systems capable of stronger interactions with a variety of adsorbates. Interestingly, back-donation interactions exhibit a mild decline in magnitude, suggesting subtle changes in metal–ligand bonding characteristics that may fine-tune the electronic environment. Finally, the more negative chemical potential values confirm a greater thermodynamic drive for electron uptake, consistent with the overall trend toward enhanced adsorption capability.

To visually corroborate these trends, Fig. 3g–i illustrates the density of states (DOS) diagrams for pristine MOF-303, Cu@MOF-303, and Ag@MOF-303, respectively. Each DOS plot is accompanied by the corresponding HOMO and LUMO orbital visualizations, allowing for a direct comparison of frontier orbital localization and energy separation. As observed, metal functionalization narrows the energy gap between HOMO and LUMO, confirming the numerical trends discussed earlier. Additionally, the HOMO and LUMO orbitals in metalated structures exhibit more delocalized and asymmetric distributions, which are indicative of increased electronic reactivity and altered charge transport pathways.

The DFT-derived electronic descriptors provide a mechanistic explanation for the enhanced water uptake observed in metal-doped MOF-303 structures. Specifically, the increase in dipole moment, electrophilicity, and electronegativity upon Cu and Ag incorporation indicates a more polarized and reactive framework that promotes stronger interactions with water molecules. For instance, the higher electron-withdrawing ability of Cu leads to more localized electrostatic potential that stabilizes water coordination, whereas the slightly more

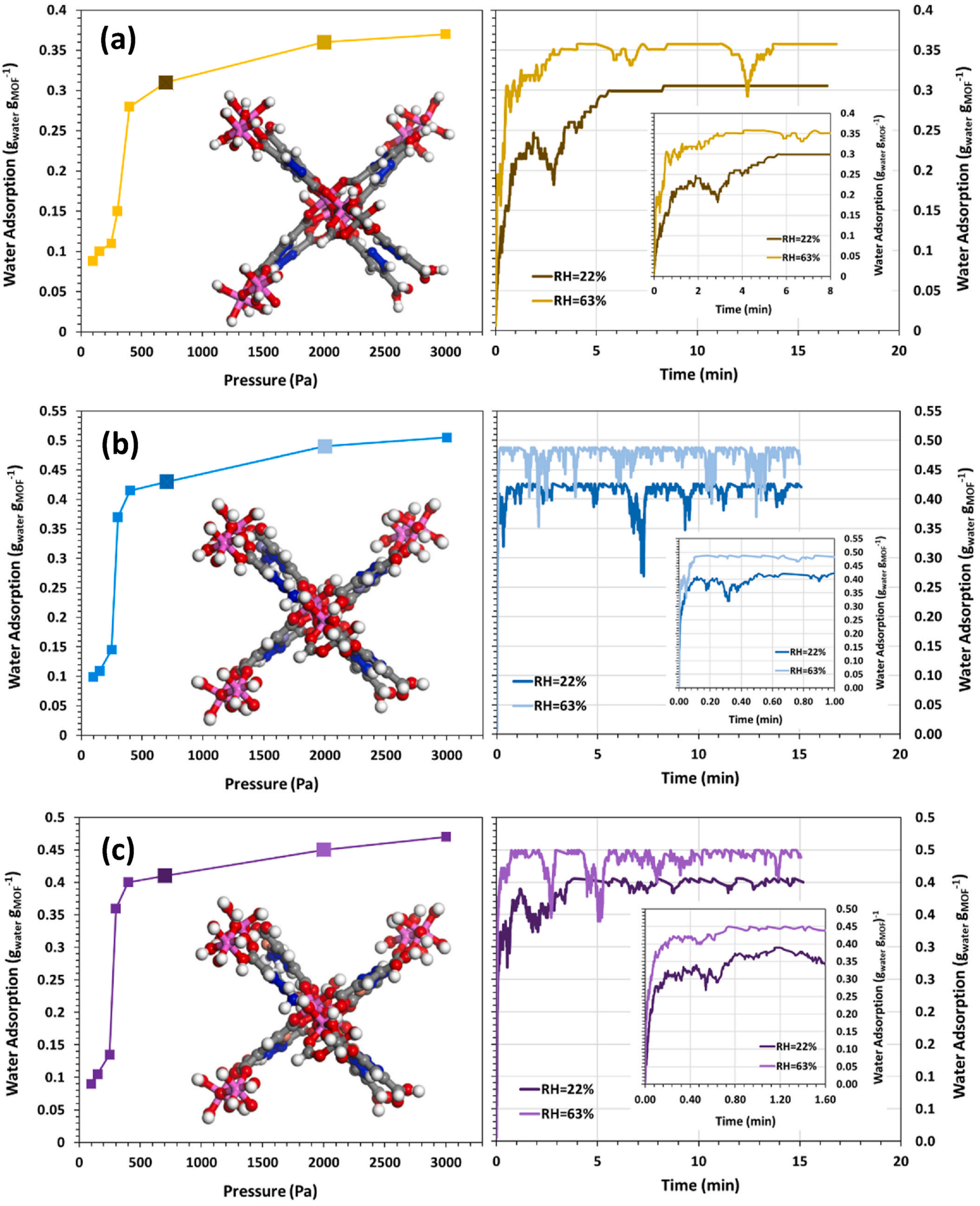

Fig. 4. Water adsorption kinetics for (a) MOF-303, (b) Cu@MOF-303, and (c) Ag@MOF-303 at 700 and 2000 Pa at 300 K.

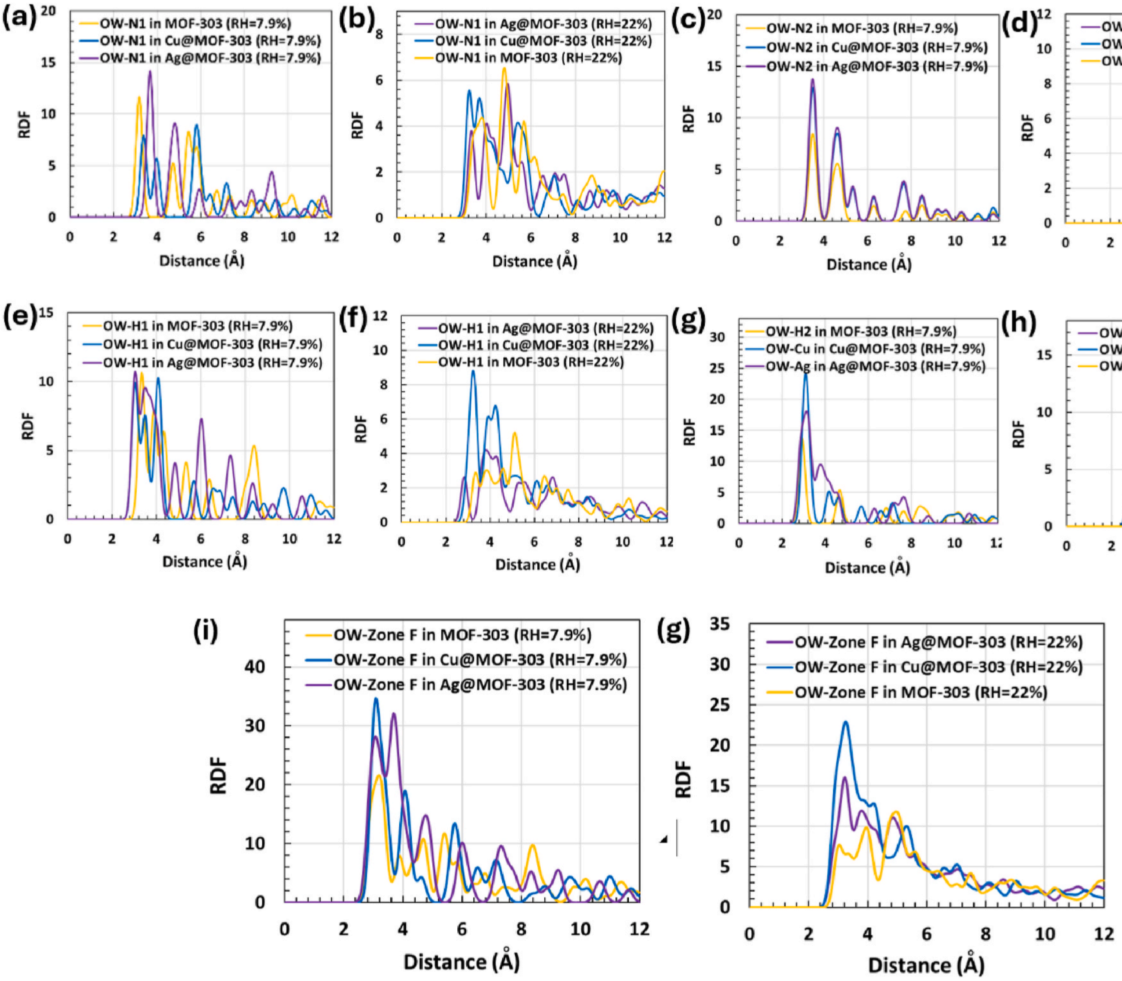

Fig. 5. RDF profiles of OW at 7.9 % and 22 % RH with (a,b) N_1, (c,d) N_2, (e,f) H_1, (g,h) X (X = H_2, Cu, Ag), and (i,g) OW with all adsorption sites in zone F, in pristine and metalated MOF-303 at 300 K.

delocalized polarization effect of Ag enhances water binding even in regions distant from the metal site. These electronic trends correspond well with the GCMC-derived adsorption isotherms and adsorption energies, offering a consistent picture of how atomic-scale electronic properties govern water structuring within the MOF pores.

To experimentally validate the predictions from our computational study, several complementary techniques could be employed. Infrared (IR) spectroscopy or diffuse reflectance infrared Fourier transform spectroscopy (DRIFTS) can detect shifts in vibrational modes of water molecules interacting with metal sites, reflecting nature and strength of adsorption. Adsorption calorimetry provides direct measurements of adsorption enthalpies, serving as a quantitative benchmark for the DFT-derived adsorption energies presented in Table 1. Furthermore, X-ray photoelectron spectroscopy (XPS) or UV–visible diffuse reflectance spectroscopy (DRS) could probe changes in electronic environments and metal oxidation states caused by metal doping, correlating with the Mulliken/NBO charge distribution and molecular electrostatic potential analyses. These experimental approaches would thus offer valuable validation and deeper insight into the electronic and adsorption behavior of metal-functionalized MOF-303 frameworks.

3.3. Kinetic behavior of water adsorption

The kinetic behavior of water adsorption at two representative pressures (700 Pa and 2000 Pa) was investigated using KMC simulations, as depicted in Fig. 4a–c for pristine and metalated MOF-303 structures. The temporal profiles clearly demonstrate a pressure-dependent acceleration in adsorption rates across all materials.

For pristine MOF-303 (Fig. 4a), the saturation time was approximately 8 min at 700 Pa and 4 min at 2000 Pa, which aligns well with prior experimental data [13], confirming the reliability of the adopted kinetic model and force field parameters. Upon Cu(I) docking (Cu@MOF-303, Fig. 4b), the adsorption kinetics were markedly accelerated, achieving saturation in only ~1.5 min at 700 Pa and less than 0.3 min at 2000 Pa. This rapid uptake is particularly valuable for atmospheric water harvesting, where performance under low humidity conditions (i.e., low partial pressure of water vapor) is crucial. A faster response at low RH translates directly into more efficient water capture during limited atmospheric exposure windows, such as at night or in arid climates. Although Ag@MOF-303 (Fig. 4c) also demonstrated improved kinetics over the pristine framework (with saturation time ~ 4 min at 700 Pa and 0.8 min at 2000 Pa), the rate enhancement was clearly inferior to that of the Cu-doped variant. The enhanced kinetics in Cu@MOF-303 can be attributed to the higher Lewis acidity of Cu(I) compared to Ag(I), which promotes stronger interactions with water molecules. This facilitates earlier nucleation and faster propagation of water clusters through the hydrophilic pore network. These kinetic results are consistent with the adsorption energy trends obtained from DFT calculations, further validating the stronger binding affinity and enhanced water uptake observed in the metalated MOF-303 structures. Compared to the pristine MOF-303, both Cu(I) and Ag(I)-modified MOF-303 exhibited significantly faster adsorption kinetics, highlighting the potential of post-synthetic metalation, particularly with Cu (I), as a strategy to optimize performance in AWH systems.

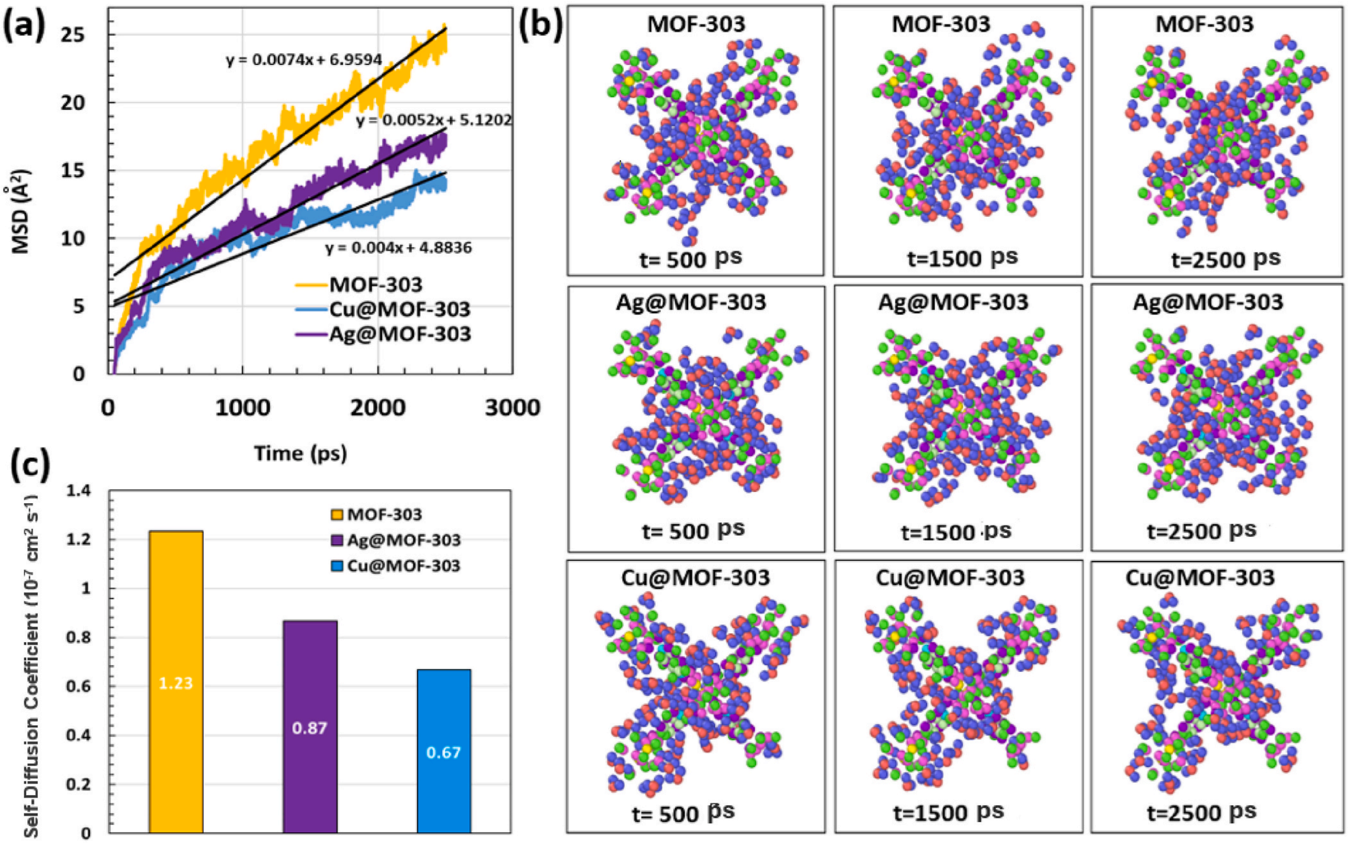

Fig. 6. (a) MSD of water molecules and (b) time-resolved distribution snapshots in pristine and metalated MOF-303 (T = 300 K, RH = 22 %), (c) Self-diffusion coefficients of water in pristine and metal-doped MOF-303 over long time regimes (300–2500 ps), as computed from MSD slopes at 300 K and RH = 22 %.

3.4. Molecular-level study

To gain molecular-level insight into the interaction between water molecules and specific adsorption sites in zone F, RDF analyses were performed at 300 K for selected atoms in contact with the oxygen of water under two RH conditions (7.9 % and 22 %). Fig. 5 illustrates these RDF profiles for both pristine and metalated MOF-303s. All cases exhibit a pronounced peak around 2.7–3.0 Å corresponding to hydrogen bonds. Also, a general trend observed across all systems is the decrease in RDF values with increasing RH. This behavior reflects the weakening of specific interactions between individual adsorption sites and water molecules as the RH level increases, likely due to competition between neighboring sites and the broader distribution of water molecules within the framework at higher RH. Interestingly, the RDF trends align closely with the partial charge distributions obtained from the Mulliken and NBO analyses shown in Fig. 5. Specifically, sites exhibiting more negative charge tend to show reduced RDF intensity, suggesting that increased electron density repels the partial negative charge of water's oxygen. Conversely, less negatively charged or slightly positive sites display enhanced RDF peaks, consistent with stronger electrostatic attraction. Moreover, metal docking significantly influences RDF behavior. The site that undergoes direct metal substitution shows a pronounced increase in RDF intensity, highlighting its enhanced affinity for water due to metal-induced polarization. Cu@MOF-303 showed the highest RDF peak intensity at ~2.8 Å, indicating more localized water structuring near the metal sites. Beyond the substituted site, metal docking also affects neighboring atoms through electronic redistribution. This is particularly evident for the N1 and H1 atoms, whose RDF profiles shift noticeably in the presence of Cu or Ag. These observations underscore the extended electronic influence of the coordinated metal centers. This redistribution reshapes water interaction patterns within Zone F.

To complement the site-specific analysis and assess the collective impact of metal docking on water uptake behavior, RDF calculations were extended to the entire zone F. This broader perspective enables evaluation of how local modifications propagate across the framework and influence the overall interaction landscape. As shown in Fig. 5i and g, a marked increase in RDF intensity is observed upon metal docking, clearly indicating that the introduction of transition metals significantly enhances the overall affinity of the framework for water molecules. This enhancement reflects the collective effect of local electronic polarization and structural rearrangement induced by metal docking, which facilitates stronger and more frequent interactions across zone F. Furthermore, a comparative analysis between the two metalated structures reveals that Cu@MOF-303 exhibits higher RDF values and sharper peak positions than Ag@MOF-303. Among the two systems studied, Cu docking proves more effective, yielding a MOF environment that is not only more reactive but also more capable of establishing strong and spatially organized interactions with water molecules. This observation is consistent with the results from earlier sections, all of which pointed to superior adsorption characteristics for the Cu-metalated MOF. Overall, these findings emphasize that metal docking-regardless of the specific metal-substantially enhances water adsorption by introducing electronic polarization and structural asymmetry into the framework.

To investigate the dynamic behavior of water molecules within the MOF structures, MSD plots were generated at 300 K and RH = 22 % for pristine and metal-docked MOF-303 systems, as shown in Fig. 6a. The results reveal that the slope of the MSD curve for the pristine MOF-303 is significantly higher than those of the metalated MOFs. This trend indicates greater mobility and weaker interaction of water molecules in the unmodified framework. In contrast, the reduced MSD slopes for Cu@MOF-303 and Ag@MOF-303 reflect increased stabilization and

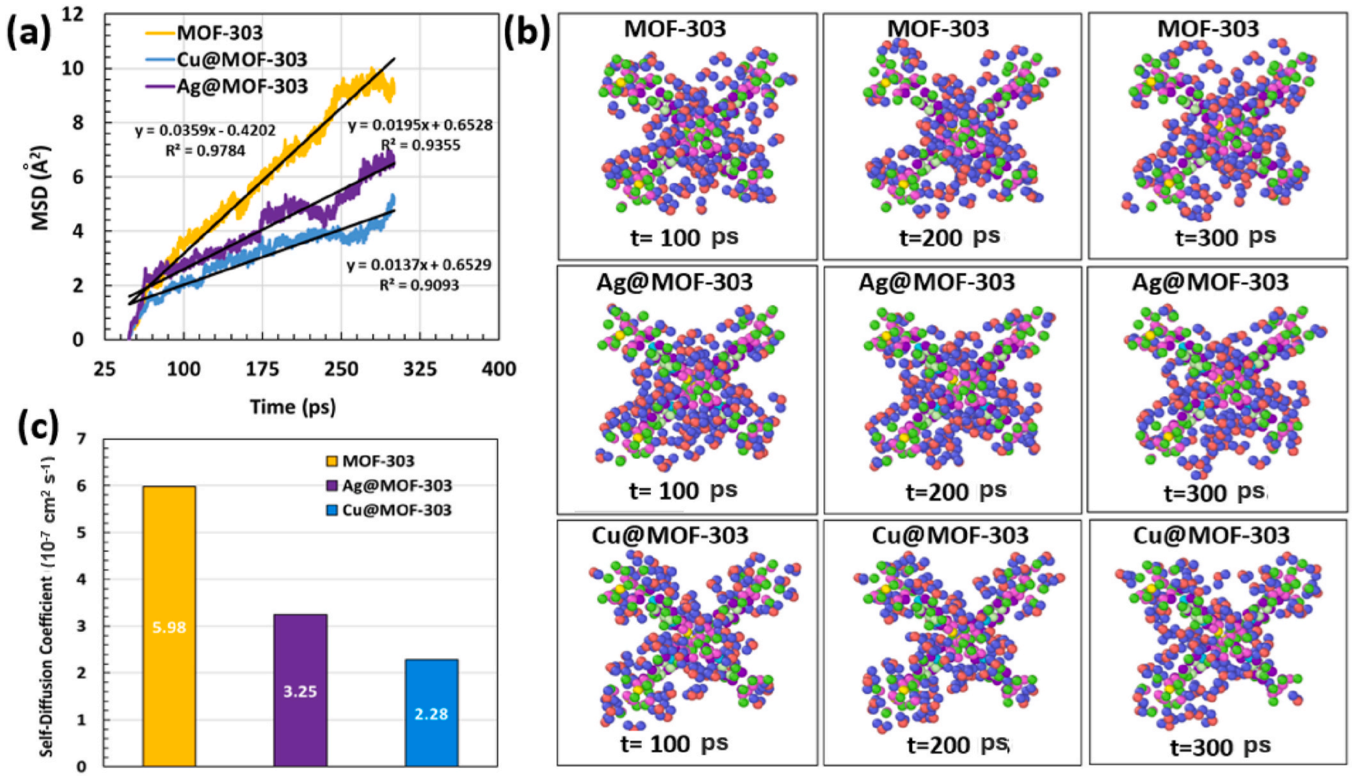

Fig. 7. (a) Early-time MSD profiles and (b) corresponding snapshots highlighting initial water stabilization in pristine and metalated MOF-303 (T = 300K RH = 22 %), (c) Self-diffusion coefficients of water in pristine and metal-doped MOF-303 over short time regimes (50–300 ps), as computed from MSD slopes at 300 K and RH = 22 %.

hindered diffusion, attributable to the stronger binding interactions facilitated by the additional adsorption sites introduced via metal docking. Notably, among the metalated systems, Ag@MOF-303 shows a slightly higher MSD slope compared to Cu@MOF-303, suggesting that water molecules experience less restriction in the silver-containing framework. This observation aligns well with the adsorption energy values obtained, reinforcing the conclusion that Cu incorporation results in stronger water binding and reduced molecular mobility.

To visualize these dynamic differences, Fig. 6b presents time-resolved snapshots of water distribution at three different time intervals. The images clearly demonstrate more extensive movement of water in the pristine MOF compared to the confined distribution seen in the metalated structures. Furthermore, water clustering appears more compact and spatially confined in Cu@MOF-303 than in Ag@MOF-303, providing qualitative support for the quantitative MSD findings.

Interestingly, closer examination of the MSD behavior during the initial simulation period reveals a different trend in displacement slope compared to the later stages. As shown in Fig. 7, early-time MSD curves, along with corresponding snapshots, exhibit an initial rapid stabilization of water molecules near the metal coordination sites. This early immobilization indicates a strong initial binding of water molecules to high-affinity regions introduced by metal docking, particularly in the Cu-containing framework. Such behavior mirrors the trends observed in KMC simulations, where early-stage kinetics are dominated by rapid occupation of the highest-affinity sites. These results provide compelling evidence that metal coordination not only enhances the thermodynamic driving force for water adsorption but also significantly impacts the kinetic landscape, restricting water mobility through stronger, site-specific interactions that manifest early during the adsorption process.

Figs. 6c and 7c presents the diffusion coefficients estimated from the linear regions of the MSD plots for all three MOF systems over two distinct time intervals: the initial phase (50–300 ps) and the later equilibrium phase (300–2500 ps). As expected, the diffusion coefficients in the early stage are significantly higher for all systems compared to their corresponding equilibrium values. This behavior reflects the rapid initial movement of water molecules before the onset of strong adsorption interactions and confinement within specific sites of the framework. Upon metal incorporation, a clear reduction in diffusion coefficients is observed across both time intervals. This trend can be attributed to the introduction of additional high-affinity adsorption sites via Cu and Ag docking, which enhances water–framework interactions and reduces molecular mobility. The overall decrease in diffusion coefficients is consistent with the observed lower MSD slopes for the metalated systems and the more localized water distributions seen in the snapshot analyses. Among the three structures, Cu@MOF-303 exhibits the lowest diffusion coefficient in both time windows, highlighting its stronger binding affinity and more effective confinement of water molecules. This finding corroborates prior evidence from RDF profiles, adsorption energies, and electronic structure analyses, all of which pointed to superior water–framework interaction strength in the Cu-docked system. In contrast, Ag@MOF-303 shows slightly higher diffusivity, reflecting relatively weaker interactions compared to Cu, but still more confined than the pristine MOF.

These results collectively demonstrate that metal docking not only enhances the thermodynamic favorability of water adsorption but also significantly modulates the kinetic behavior of water transport within the MOF structure. The observed reduction in diffusivity, particularly in Cu@MOF-303, serves as an indicator of stronger and more localized adsorption sites. This pronounced molecular confinement is highly advantageous for atmospheric water harvesting applications, where efficient capture, retention, and controlled release of water vapor are essential for maximizing harvesting efficiency under varying humidity conditions.

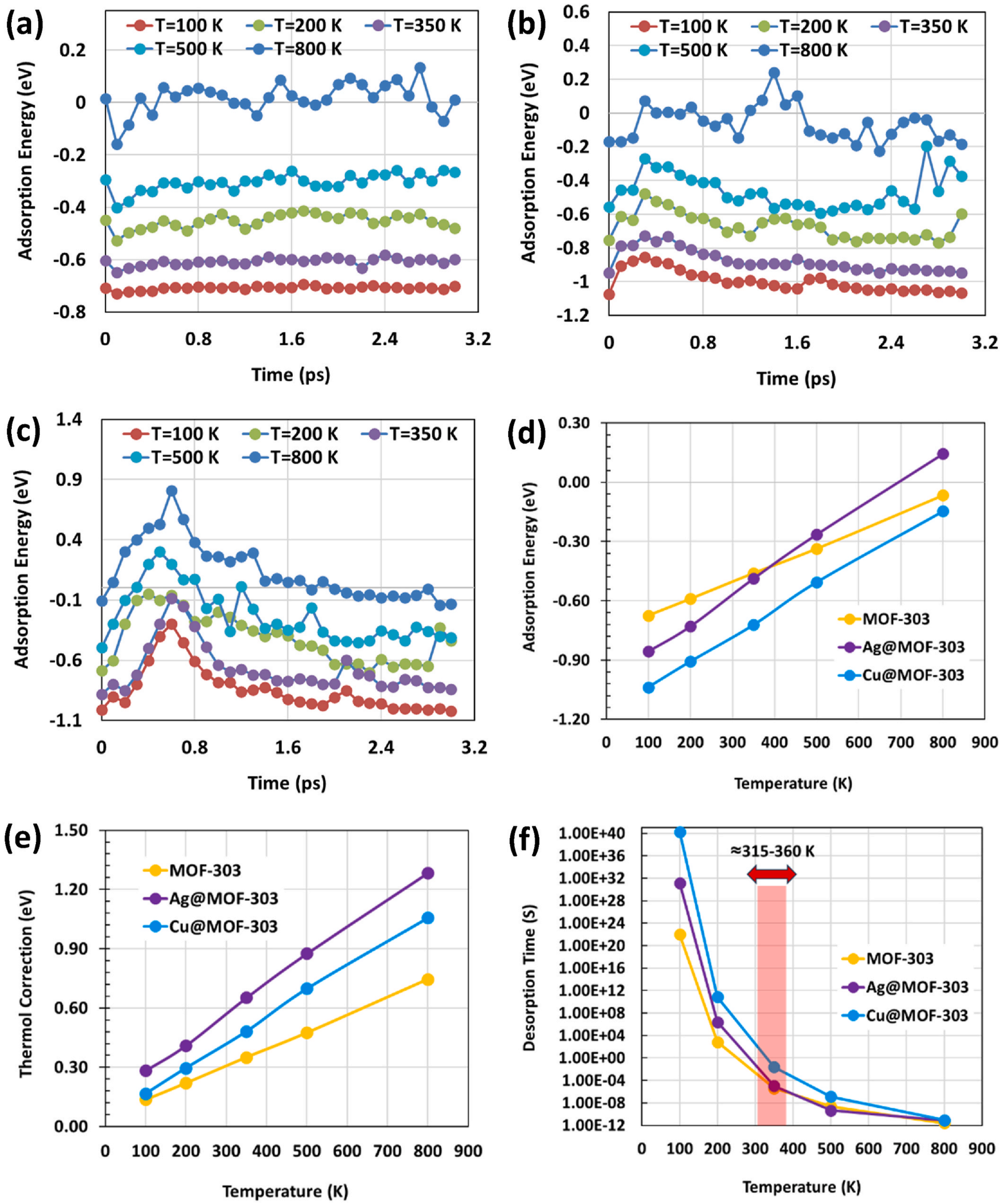

Fig. 8. (a–c) Time-dependent fluctuations in adsorption energies at various temperatures (100–800 K) for MOF-303, Cu@MOF-303, and Ag@MOF-303, respectively. (d) Average adsorption energies of H_2O across the same temperature range for all three structures. (e) Corresponding thermal corrections of adsorption energies. (f) Estimated desorption time constants (τ) as a function of temperature, with the practical AWH-relevant desorption window (315–360 K) highlighted in red. (For interpretation of the references to color in this figure legend, the reader is referred to the Web version of this article.)

3.5. Desorption kinetic study

Understanding the desorption behavior of water molecules is critical for evaluating the practical applicability of MOF-based adsorbents in AWH, where a high water uptake must be balanced with desorption at moderate temperatures to ensure energy-efficient recovery. If water release requires excessively high temperatures, the real-world viability of the material is significantly reduced.

Fig. 8a–c shows the time-dependent fluctuation of adsorption energies for MOF-303, Cu@MOF-303, and Ag@MOF-303, respectively, at various temperatures (100, 200, 350, 500, and 800 K). It should be noted that temperature values above the critical point of water (647 K) were included only to extend the mathematical trend of the Polanyi-Wigner relation and do not correspond to real adsorption states. In all three cases, the amplitude of fluctuations increases with temperature, indicating greater dynamic instability at higher thermal energy. Furthermore, the metalated structures exhibit overall higher fluctuation amplitudes than pristine MOF-303, with Ag@MOF-303 showing the most pronounced variations across all temperatures.

Fig. 8d shows average temperature-dependent adsorption energies of H_2O on pristine and metalated MOF-303 were computed over a temperature range of 100–800 K. As temperature increases, the adsorption energies for all three structures shift progressively from negative values toward zero, indicating reduced water affinity. This shift is notably steeper for Ag@MOF-303 and Cu@MOF-303 compared to the pristine framework, reflecting a stronger thermal sensitivity in the metalated systems.

Thermal correction values for adsorption energies were also computed and are illustrated in Fig. 8e. For all three structures, thermal correction increases with temperature. However, the metalated structures exhibit steeper slopes and greater magnitudes of thermal correction compared to the pristine MOF-303. Among them, Ag@MOF-303 shows the highest degree of temperature-dependent change in thermal correction.

The adsorption energies obtained from DFT after applying thermal corrections were compared with approximated adsorption energies obtained from the ensemble-averaged potential energy in GCMC simulations at 300 K (Table S4). Despite the inherent methodological differences between DFT and GCMC approaches, both sets of results exhibit similar trends, supporting the validity of the thermal correction procedure and the overall multiscale modeling framework.

Based on energy values illustrated in Fig. 8d, the desorption time constant (τ) was calculated using Eq. (7) and plotted in Fig. 8f. Here, the τ characterizes the rate at which adsorbed water molecules leave the framework; a smaller τ indicates a faster desorption process, which is more conducive to rapid water recovery and energy-efficient operation in practical AWH systems. As expected, τ decreases with rising temperature for all structures. Experimental studies indicate that desorption from MOF-303 typically occurs between 315 and 360 K (shaded in red in Fig. 8f) [13,74]. Within this temperature window, Cu@MOF-303 shows significantly longer desorption times relative to Ag@MOF-303 and the pristine form. At 350 K, for example, τ values are 4.18×10^{-6} s (pristine), 1.05×10^{-5} s (Ag@MOF-303), and 2.47×10^{-2} s (Cu@MOF-303). Taking the behavior of pristine MOF-303 at 350 K as a reference, where water desorption occurs with a characteristic time constant of approximately 4.18×10^{-6} s, one can estimate the equivalent temperatures required for the functionalized materials to reach similar desorption performance. Based on this, Ag@MOF-303 would need to reach 367 K, and Cu@MOF-303 approximately 460 K.

While Cu@MOF-303 exhibited superior water uptake and faster adsorption kinetics, its delayed desorption suggests poor regeneration efficiency under solar-driven or low-grade heat conditions common in AWH systems. In contrast, Ag@MOF-303 not only enhanced water uptake relative to the pristine MOF-303 but also maintains a desorption profile closely aligned with it, offering a more favorable balance between performance and energy efficiency. These findings highlight Ag@MOF-303 as a more suitable candidate for real-world AWH applications.

4. Conclusions and broader impact

This study revealed how post-synthetic metalation of MOF-303 with Cu(I) and Ag(I) modifies the thermodynamic, electronic, and dynamic properties relevant to water adsorption-desorption. The integrated multiscale simulation framework established in this study enabled a complete and self-consistent description of the AWH cycle, from adsorption to desorption. DFT calculations provided quantum-level parameters such as partial charges, binding energies, and optimized metal-water geometries, which served as input for GCMC, KMC, and MD simulations. Using these parameters, GCMC quantified macroscopic adsorption isotherms across humidity levels, KMC captured time-dependent adsorption and desorption kinetics, and MD elucidated molecular diffusion and structural dynamics within the pores. Finally, thermodynamic analyses of temperature-dependent adsorption energies completed the full adsorption-desorption cycle, linking molecular-scale energetics to macroscopic regeneration behavior. Under ultra-low humidity conditions (∼10 % RH), pristine MOF-303 exhibits a limited water uptake of about 0.15 g g^{-1}. In contrast, Ag@MOF-303 and Cu@MOF-303 display substantially enhanced adsorption capacities of approximately 0.367 g g^{-1} and 0.372 g g^{-1}, corresponding to 145 % and 148 % increases, respectively, compared to the unmodified framework. Beyond this low-humidity regime, Cu@MOF-303 further demonstrates an approximately 37 % higher saturation uptake and noticeably slower water diffusion, resulting from stronger binding energies and more localized electrostatic fields around the Cu sites. Similarly, Ag@MOF-303 shows a ∼27 % enhancement in saturation uptake relative to pristine MOF-303 while maintaining comparable desorption behavior, offering a favorable balance between adsorption capacity and regeneration efficiency for practical AWH applications. Although Cu@MOF-303 outperforms in uptake and kinetics, its slower regeneration under moderate thermal input may limit its applicability in solar-powered systems. In contrast, our temperature-dependent adsorption energy analysis showed that Ag@MOF-303 maintains desorption behavior closely aligned with the pristine MOF-303. This distinction highlights Ag@MOF-303's superior suitability for off-grid and SAWH systems, where low thermal input is preferred. These findings not only underscore the critical role of local polarization and charge redistribution in enhancing both water uptake capacity and adsorption kinetics but also highlight the importance of desorption behavior as a determining factor for the practical viability of MOFs in AWH applications.

This methodological integration confirms that the observed adsorption capacity and desorption efficiency originate from coherent interactions across electronic, kinetic, and dynamic scales, highlighting the robustness and predictive capability of the proposed multiscale approach. Future work should explore other high-polarity metals (e.g., Fe^{3+}, Zn^{2+}) and validate simulation predictions experimentally. Integrating these insights into high-throughput or device-level simulations could accelerate the design of MOFs for atmospheric water harvesting in arid climates.

CRediT authorship contribution statement

Mehrzad Arjmandi: Writing – review & editing, Writing – original draft, Visualization, Validation, Software, Methodology, Investigation, Formal analysis, Data curation, Conceptualization. **Mohamed Khayet:** Writing – review & editing, Writing – original draft, Visualization, Validation, Supervision, Software, Resources, Project administration, Methodology, Investigation, Funding acquisition, Formal analysis, Data curation, Conceptualization. **Sofia Calero:** Writing – review & editing, Visualization, Validation, Methodology, Investigation, Data curation, Conceptualization.

Declaration of competing interest

The authors declare that they have no known competing financial interests or personal relationships that could have appeared to influence the work reported in this paper.

Acknowledgement

This work was supported by the European Union under the Marie Skłodowska-Curie Actions (MSCA), HORIZON-MSCA-2023-PF-01-01, through the PHOTOWAT project (Grant Agreement No. 101154984, DOI: 10.3030/101154984), coordinated by University Complutense of Madrid (UCM), Spain.

Appendix A. Supplementary data

Supplementary data to this article can be found online at https://doi.org/10.1016/j.micromeso.2025.113943.

Data availability

Data will be made available on request.

References

[1] W.A. Jury, V. H. J Jr., The emerging global water crisis: managing scarcity and conflict between water users, Adv. Agron. 95 (2007) 1–76.

[2] B. Tashtoush, A. Alshoubaki, Atmospheric water harvesting: a review of techniques, performance, renewable energy solutions, and feasibility, Energy 280 (2023) 128186.

[3] C. Zeng, A. Mojiri, J. Ananpattarachai, A. Farsad, P. Westerhoff, Sorption-based atmospheric water harvesting for continuous water production in the built environment: assessment of water yield and quality, Water Res. 265 (2024) 122227.

[4] Y. Hu, Z. Ye, X. Peng, Metal-organic frameworks for solar-driven atmosphere water harvesting, Chem. Eng. J. 452 (2023) 139656.

[5] M. Arjmandi, E. Aytaç, M. Khayet, N. Hilal, Next-generation MOFs for atmospheric water harvesting: the role of machine learning techniques, Coord. Chem. Rev. 548 (2025) 217211.

[6] S. Devautour-Vinot, G. Maurin, C. Serre, P. Horcajada, D.P.d. Cunha, V. Guillerm, E.d.S. Costa, F. Taulelle, C. Martineau, Structure and dynamics of the functionalized MOF Type UiO-66(Zr): NMR and dielectric relaxation spectroscopies coupled with DFT calculations, Chem. Mater. 24 (2012) 2168–2177.

[7] S. Kavak, D. Jannis, A.D. Backer, D.A. Esteban, A. Annys, S. Carrasco, J. Ferrando-Ferrero, R.M. Guerrero, P. Horcajada, J. Verbeeck, S.B. Sandra Van Aert, High-resolution electron microscopy imaging of MOFs at optimized electron dose, J. Mater. Chem. A 13 (2025) 4281–4291.

[8] M. Giménez-Marqués, E. Bellido, T. Berthelot, T. Simón-Yarza, T. Hidalgo, R. Simón-Vázquez, Á. González-Fernández, J. Avila, M.C. Asensio, R. Gref, P. Couvreur, C. Serre, P. Horcajada, Metal-Organic framework surface functionalization: graftfast surface engineering to improve MOF nanoparticles furtiveness, Small 14 (2018) 1870182.

[9] E. Binaeian, N. Motaghedi, S. Maleki, M. Arjmandi, Ibuprofen uptake through dimethyl ethylenediamine modified MOF: optimization of the adsorption process by response surface methodology technique, J. Dispersion Sci. Technol. 43 (2020) 1–14.

[10] Y. Li, J. Yu, Y. Li, J. Shen, M. Du, X. Zhang, H. Zhao, J.H. Pu, Nanoporous MOF-303 performance for atmospheric water harvesting in the presence of airborne contaminants: GCMC and DFT simulations, ACS Appl. Nano Mater. 7 (2024) 23850–23859.

[11] F. Fathieh, M.J. Kalmutzki, E.A. Kapustin, P.J. Waller, J. Yang y O.M. Yaghi, Practical water production from desert air, Sci. Adv. 4 (2018) eaat3198.

[12] N. Hanikel, D. Kurandina, S. Chheda, Z. Zheng, Z. Rong, S.E. Neumann, J. Sauer, J. I. Siepmann, L. Gagliardi, O.M. Yaghi, MOF linker extension strategy for enhanced atmospheric water harvesting, ACS Cent. Sci. 9 (2023) 551–557.

[13] N. Hanikel, M.S. Prévot, F. Fathieh, E.A. Kapustin, H. Lyu, H. Wang, N.J. Diercks, T.G. Glover, O.M. Yaghi, Rapid cycling and exceptional yield in a metal-organic framework water harvester, ACS Cent. Sci. 5 (2019) 1699–1706.

[14] Z. Zheng, H.L. Nguyen, N. Hanikel, K.K.-Y. Li, Z. Zhou, T. Ma, O.M. Yaghi, High-yield, green and scalable methods for producing MOF-303 for water harvesting from desert air, Nat. Protoc. 18 (2023) 136–156.

[15] M. Arjmandi, M.P. Chenar, M. Peyravi, M. Jahanshahi, Influence of As-Formed metal-oxide in non-activated water-unstable organometallic framework pores as hydrolysis delay agent: interplay between experiments and DFT modeling, J. Inorg. Organomet. Polym. Mater. 29 (2019) 178–191.

[16] H. Wang, D.Z. Shi, D.J. Yang, T. Sun, B. Rungtaweevoranit, H. Lyu, Y.-B. Zhang, O. M. Yaghi, Docking of CuI and AgI in metal–organic frameworks for adsorption and separation of xenon, Angew. Chem. Int. Ed. 15 (2021) 3417–3421.

[17] H.-Y. Li, X.-J. Kong, S.-D. Han, J. Pang, G.-M.W. Tao He, X.-H. Bu, Metalation of metal–organic frameworks: fundamentals and applications, Chem. Soc. Rev. 53 (2024) 5626–5676.

[18] Y. Pan, Y. Wang, D. Wang, H. Ma, G. Wang, Post-docking hydrophilic Ag-MOF-303 filled in TFC for nanofiltration of charged PhACs in water, Chem. Eng. J. 502 (2024) 158027.

[19] M. Li, X. Wang, J. Zhang, Y. Gao, W. Zhang, Cu-loaded MOF-303 for iodine adsorption: the roles of Cu species and pyrazole ligands, Appl. Surf. Sci. 619 (2023) 156819.

[20] C.R. Groom, I.J. Bruno, M.P. Lightfoot, S.C. Ward, The Cambridge structural database, Acta Crystallogr. B: Structural Science, Crystal Engineering and Materials 72 (2016) 171–179.

[21] G. Yang, C. Jin, J. Hong, Z. Guo, L. Zhu, Ab initio and density functional theory studies on vibrational spectra of palladium (II) and platinum (II) complexes of methionine and histidine: effect of theoretical methods and basis sets, Spectrochim. Acta Mol. Biomol. Spectrosc. 60 (2004) 3187–3195.

[22] S.F. Sousa, G.R.P. Pinto, A.J.M. Ribeiro, J.T.S. Coimbra, P.A. Fernandes, M. J. Ramos, Comparative analysis of the performance of commonly available density functionals in the determination of geometrical parameters for copper complexes, J. Comput. Chem. 34 (2013) 2079–2090.

[23] S. Chiodo, N. Russo y E. Sicilia, LANL2DZ basis sets recontracted in the framework of density functional theory, J. Chem. Phys. 125 (2006) 104107.

[24] T. Tavare, D.P.E. Motta, A. Carpanez, M. Lopes, E. Fontes, H.D. Santos, H. Silva, R. Grazul, A. Fontes, Platinum(II) and palladium(II) aryl-thiosemicarbazone complexes: synthesis, characterization, molecular modeling, cytotoxicity, and antimicrobial activity, J. Coord. Chem. 67 (2014) 956–968.

[25] M. Arjmandi, M. Peyravi, M.P. Chenar, M. Jahanshahi, A. Arjmandi, Study of adsorption of H_2 and CO_2 on distorted structure of MOF-5 framework; A comprehensive DFT study, Journal of Water and Environmental Nanotechnology 3 (2018) 70–80.

[26] M. Peyravi, M. Arjmandi, R. Khakpour, M. Jahanshahi, A chemisorption study of selenium dioxide on C19X (X= Ni, Cr and Cu) nanocage by DFT-based calculation, Surf. Interfaces 16 (2019) 174–180.

[27] F.H.K. Djioko, C.G. Fotsop, G.K. Youbi, S.C. Nwanonenyi, C.A. Madu, E.E. Oguzie, Unraveling the sorption mechanisms of ciprofloxacin on the surface of zeolite 4A (001) in aqueous medium by DFT and MC approaches, Appl. Surf. Sci. Adv. 19 (2024) 100542.

[28] E. Louis, E. San-Fabián, M.A. Díaz-García, G. Chiappe, J.A. Vergés, Are electron affinity and ionization potential intrinsic parameters to predict the electron or hole acceptor character of amorphous molecular materials? J. Phys. Chem. Lett. 8 (2017) 2445–2449.

[29] M. Arjmandi, A. Arjmandi, M. Peyravi, A.K. Pirzaman, First-Principles Study of adsorption of XCN (X = F, Cl, and Br) on surfaces of polyaniline, Russ. J. Phys. Chem. A 94 (2020) 2148–2154.

[30] D. Dubbeldam, S. Calero, D.E. Ellis, R.Q. Snurr, «RASPA: molecular simulation software for adsorption and diffusion in flexible nanoporous materials, Mol. Simul. 42 (2015) 81–101.

[31] S. Kancharlapalli, R.Q. Snurr, High-Throughput screening of the CoRE-MOF-2019 database for CO2 capture from wet flue gas: a multi-scale modeling strategy, ACS Appl. Mater. Interfaces 15 (2023) 28084–28092.

[32] S.L. Mayo, B.D. Olafson, W.A. Goddard, DREIDING: a generic force field for molecular simulations, J. Phys. Chem. 94 (1990) 8897–8909.

[33] A.K. Rappe, C.J. Casewit, K.S. Colwell, W.A. Goddard III, W.M. Skiff, UFF, a full periodic table force field for molecular mechanics and molecular dynamics simulations, J. Am. Chem. Soc. 114 (1992) 10024–10035.

[34] H.J.C. Berendsen, J.R. Grigera, T.P. Straatsma, The missing term in effective pair potentials, J. Phys. Chem. 91 (1987) 6269–6271.

[35] J. Yu, M.L. Sushko, S. Kerisit, K.M. Rosso, J. Liu, Kinetic Monte Carlo Study of ambipolar Lithium ion and electron–polaron diffusion into nanostructured TiO2, J. Phys. Chem. Lett. 3 (2012) 2076–2081.

[36] M. Shirazi, S.D. Elliott, Atomistic kinetic Monte Carlo study of atomic layer deposition derived from density functional theory, J. Comput. Chem. 35 (2014) 244–259.

[37] F. Pieck, R. Tonner-Zech, Computational Ab initio approaches for area-selective atomic layer deposition: methods, status, and perspectives, Chem. Mater. 37 (2025) 2979–3021.

[38] N. Dawass, J. Langeveld, M. Ramdin, E. Pérez-Gallent, A.A. Villanueva, E.J. M. Giling, J. Langerak, L.J. P.v. d. Broeke, T.J.H. Vlugt, O.A. Moultos, Solubilities and transport properties of CO2, oxalic acid, and formic acid in mixed solvents composed of deep eutectic solvents, methanol, and propylene carbonate, J. Phys. Chem. B 126 (2022) 3572–3584.

[39] G. Jajko, J.J. Gutiérrez-Sevillano, A. Sławek, M. Szufla, P. Kozyra, D. Matoga, W. Makowski, S. Calero, Water adsorption in ideal and defective UiO-66 structures, Microporous Mesoporous Mater. 330 (2022) 111555.

[40] J. Vicent-Luna, J. Romero-Enrique, S. Calero, J. Anta, Micelle Formation in aqueous solutions of room temperature ionic liquids: a molecular dynamics Study, J. Phys. Chem. B 121 (2017) 8348–8358.

[41] M.C. Bessa, A. Luna-Triguero, J.M. Vicent-Luna, P.M. Carmo, M.N. Tsampas, A. M. Ribeiro, A.E. Rodrigues, S. Calero, A.F. Ferreira, An efficient strategy for electroreduction reactor outlet fractioning into valuable products, Ind. Eng. Chem. Res. 62 (2023) 8847–8863.

[42] Z. Liu, Q. Cheng, K. Li, Y. Wang, J. Zhang, The interaction of nanoparticulate Fe2O3 in the sintering process: a molecular dynamics simulation, Powder Technol. 367 (2020) 97–104.

[43] R. Réocreux, C. Michel, P. Fleurat-Lessard, P. Sautet, S.N. Steinmann, Evaluating thermal corrections for adsorption processes at the Metal/Gas interface, J. Phys. Chem. C 123 (2019) 28828–28835.
[44] P. Atkins, J.d. Paula, in: Atkins' Physical Chemistry, eighth ed., Oxford University Press, 2006.
[45] R.F. Sekerka, Grand Canonical Ensemble,» De *Thermal Physics (Thermodynamics and Statistical Mechanics for Scientists and Engineers)*, Elsevier, 2015, pp. 359–396.
[46] M. Aschi, F. Grandinetti, The ionization potential of NF3: a G3 computational study on the thermochemical properties of NFx and NFx+ (x=1–3), J. Mol. Struct.: THEOCHEM 497 (2000) 205–209.
[47] S. Peng, K. Cho, P. Qi, H. Dai, Ab initio study of CNT NO2 gas sensor, Chem. Phys. Lett. 387 (2004) 271–276.
[48] L. Bai, Z. Zhou, Computational study of B- or N-doped single-walled carbon nanotubes as NH3 and NO2 sensors, Carbon 45 (2007) 2105–2110.
[49] K.A. Fichthorn, K.E. Becker, R.A. Miron, Molecular simulation of temperature-programmed desorption, Catal. Today 123 (2007) 71–76.
[50] X. Deng, T. Gao, J. Dai, Temperature dependence of adsorption and desorption dynamics of NO_2 molecule on boron-doped graphene, Phys. E Low-dimens. Syst. Nanostruct. 137 (2022) 115083.
[51] N. Hanikel, X. Pei, H.L. Saumil Chheda, W. Jeong, J. Sauer, L. Gagliardi, O. M. Yaghi, Evolution of water structures in metal-organic frameworks for improved atmospheric water harvesting, Science 374 (2021) 454–459.
[52] V.N. Mikhaylov, I.V. Kazakov, T.N. Parfeniuk, O.V. Khoroshilova, M. Scheer, A. Y. Timoshkin, I.A. Balova, The carbene transfer to strong Lewis acids: copper is better than silver, Dalton Trans. 2 (2004) 3044–3049.
[53] K. Iyanar, M.P. Sibi, Copper-based Chiral Lewis Acids,» De *Chiral Lewis Acids in Organic Synthesis*, WILEY, 2017, pp. 103–135.
[54] I. Langmuir, The ADSORPTION OF gases on plane SURFACES OF GLASS, MICA and PLATINUM, J. Am. Chem. Soc. 40 (1918) 1361–1403.
[55] R. Sips, On the structure of a catalyst surface, J. Chem. Phys. 16 (1948) 490–495.
[56] J. Tóth, Calculation of the BET-Compatible surface area from any type I isotherms measured above the critical temperature, J. Colloid Interface Sci. 225 (2000) 378–383.
[57] A. Das, R. Yadav, The influence of transition metal (Mn, Fe, Co, Cu) doping on the electronic and vibrational properties of indium nitride nanocage: a DFT study, Computational and Theoretical Chemistry 1205 (2021) 113447.
[58] S.H. Sumrra, F. Mushtaq, F. Ahmad, R. Hussain, W. Zafar, M. Imran, M.N. Zafar, Coordination behavior, structural, statistical and theoretical investigation of biologically active metal-based isatin compounds, Chem. Pap. 76 (2022) 3705–3727.
[59] H.M.A. El-Lateef, M.M. Khalaf, M. Kandeel, A.A. Amer, A.A. Abdelhamid, A. Abdou, New mixed-ligand thioether-quinoline complexes of nickel(II), cobalt (II), and copper(II): Synthesis, structural elucidation, density functional theory, antimicrobial activity, and molecular docking exploration, Appl. Organomet. Chem. 37 (2023) e7134.
[60] M.A. Akl, M.M.H. Al-Awadhi, A.S. El-Zeny, Divalent transition metal complexes of nitrogen, oxygen and sulfur containing ligand: design, structural, spectral, pH-metric, theoretical molecular modeling, analytical and mechanism studies, Appl. Water Sci. 13 (2023).
[61] A.S.M. Al-Janabi, A.O. Elzupir, M.M. Abou-Krisha, T.A. Yousef, New dual inhibitors of SARS-CoV-2 based on metal complexes with schiff-base 4-Chloro-3-Methyl phenyl hydrazine: Synthesis, DFT, antibacterial properties and molecular docking studies, INORGA 11 (2023).
[62] R.A. Al-Balushi, M.S.H. Faizi, M. Mushtaque, I.J. Al-Busaidi, M.S. Khan, Synthesis, characterization, and structural studies of some Homo- and heteroleptic Cu(I) complexes bearing 6,6′-Bis(phenylethynyl)-2,2′-Bipyridine ligand, inorganics 13 (2025).
[63] R.K. Hussein, A.M. El-Khayatt, O.K.A. Duaij, A.M. Alkaoud, Studying the biological activity of Trans-[Cu (quin)2(EtOH)2] as potent antimicrobial Cu(II) complex through computational investigations: DFT, ADMET and molecular docking, Frontiers in Bioscience-Landmark 28 (2023).
[64] M.M. Khalaf, H.M.A. El-Lateef, A. Abdou, Synthesis, structural, biological applications, DFT, molecular docking studies on Fe(III), Co(II), and Ni(II) complexes incorporating 2-(pyridin-2-yl)phenol and 1H-benzimidazole-2-carboxylic acid, Appl. Organomet. Chem. 38 (2024) e7661.
[65] B. Fresch, F. Remacle, Tuning the properties of Pd nanoclusters by ligand coatings: electronic structure computations on Phosphine, Thiol, and mixed Phosphine–Thiol ligand shells, J. Phys. Chem. C 118 (2014) 9790–9800.
[66] L. Liu, A. Corma, Bimetallic sites for catalysis: from binuclear metal sites to bimetallic nanoclusters and nanoparticles, Chem. Rev. 123 (2023) 4855–4933.
[67] Q. Lai, Y. Dou, C.-P. Tsui, M. Qi, Q. Zhang, Y. Zhu, X. Li, C.-Y. Tang, Y. Yang, Atomic Sn clusters engineered electron-deficient carbon nanofibers enable bulk-interface synergy for high-capacity and durable lithium-ion batteries, Nano Energy 129 (2025) 110987.
[68] G. Levita, P. Restuccia, M. Righi, Graphene and MoS2 interacting with water: a comparison by ab initio calculations, Carbon 107 (2016) 878–884.
[69] Z. Song, J. Fan, H. Xu, Strain-induced water dissociation on supported ultrathin oxide films, Sci. Rep. 6 (2016) 22853.
[70] L. Chen, L. Qian, Role of interfacial water in adhesion, friction, and wear—A critical review, Friction 9 (2021) 1–28.
[71] S. Meng, E. Wang, Water Adsorption on Non-metallic Surfaces,» *Water*, Springer, 2023, pp. 201–226.
[72] J.G. Brandenburg, A. Zen, M. Fitzner, B. Ramberger, G. Kresse, T. Tsatsoulis, A. Grüneis, A. Michaelides, D. Alfè, Physisorption of water on graphene: subchemical accuracy from many-body electronic structure methods, J. Phys. Chem. Lett. 10 (2019) 358–368.
[73] A. Tamtögl, E. Bahn, M. Sacchi, J. Zhu, D.J. Ward, A.P. Jardine, S.J. Jenkins, P. Fouquet, J. Ellis, W. Allison, «Motion of water monomers reveals a kinetic barrier to ice nucleation on graphene, Nat. Commun. 12 (2021).
[74] M.S. Kang, I. Heo, S.H. Park, J. Bae, S. Kim, G. Kim, B.-H. Kim, N.C. Jeong, W. C. Yoo, Time-efficient atmospheric water harvesting using Fluorophenyl oligomer incorporated MOFs, Nat. Commun. 15 (2024).